Sintering of bimodal micrometre/nanometre iron powder compacts - A master sintering curve approach

Powder Technology 391 (2021) 557–568

Contents lists available at ScienceDirect

Powder Technology

journal homepage: www.elsevier.com/locate/powtec

Sintering of bimodal micrometre/nanometre iron powder compacts - A master sintering curve approach

Swathi K. Manchili *, Johan Wendel, Eduard Hryha, Lars Nyborg

Department of Industrial and Materials Science, Chalmers University of Technology, Gothenburg SE-41258, Sweden

ARTICLE INFO

Article history:
Received 9 March 2021
Received in revised form 14 June 2021
Accepted 29 June 2021
Available online 01 July 2021

Keywords:
Nanopowder
Water atomized ferrous powder
Compaction
Sintering
Dilatometer
Master sintering curve

ABSTRACT

Though press and sinter powder metallurgy (PM) steel offers cost-effective solutions for structural applications, there is a constant drive for improvement in their density. Addition of nanopowder to the conventional micrometre-sized metal powder is explored to improve the sinter density. In this study, the effect of nanopowder addition in varying amounts has been studied. Carbonyl iron powder (<5 μm) and water atomized iron powder (<45 μm) were used as the base powder to which varying amounts of iron nanopowder (<100 nm) was added. Dilatometric sintering studies under pure hydrogen atmosphere were carried out to analyze the densification behavior. The results revealed that the bimodal powder mixture containing 25% nanopowder exhibited the highest green density for both carbonyl and ASC 300 compacts. Master sinter curve for compacts was developed based on the dilatometer data. The apparent activation energy for sintering decreased with an increase in nanopowder content. This is reflected in the values of work of sintering.

1. Introduction

To manufacture structural components through powder metallurgy (PM), the press and sinter route has been shown as a cost-effective solution for large volume production. In order to expand the usage of PM steel to applications where there is a demand for higher performance, e.g. highly-loaded structural parts, the relative sintered density must be improved [1]. There are different ways to improve the density of the compact: increasing the compaction pressure, increasing the sintering temperature or by addition of sintering aids, like in the case of liquid phase sintering. It is known that nanopowder can provide various benefits like decrease in sintering temperature and increase in mechanical properties owing to the fine grain size [2]. Nanopowder additions to powder injection molding, have shown to assist in producing dense parts at lower sintering temperatures, due to the lower activation energy required to sinter nanopowder [3]. However, at the same time, nanopowder can be associated with problems such as agglomeration, decrease in powder flowability and the high specific surface energy also makes it susceptible to oxygen pick-up, apart from the high cost associated with nanopowder [4]. Also, its addition can contribute to high interparticle friction decreasing the packing density, and together with agglomeration, inducing defects in green components [5]. Owing to these factors, not many studies have been devoted to exploring the efficacy and impact of nanopowder addition in press and sinter of water atomized powder steel. The authors have studied the influence of addition of nanopowder to micrometre-sized water atomized iron powder in detail elsewhere [6], whereby it was shown that the nanopowder showed shrinkage at temperatures as low as 500 °C. The fractographic analysis on the compacts that were sintered at temperatures like 500 and 700 °C, revealed that the nanopowder in a bimodal powder compact showed no signs of sinter bonding at 500 °C, while significant sinter bond necks had formed at 700 °C.

Sintering is the crucial stage in the manufacturing of various PM components as it sets the final properties and controls the final dimensions. During sintering, discrete particles of a porous body undergo thermal consolidation in order to reduce the surface energy by forming a dense product [7]. Sintered density of a component, being a fundamental property, influences the performance as the physical and mechanical properties are directly related to it. Thus, the processing parameters like compaction pressure and sintering temperature play an important role and for the same reason understanding of the overall densification process becomes crucial. Based on classical models for sintering developed by Kingery et al. [8] and Coble [9], various models for predicting density have been proposed. One of the widely used models is the so called master sintering curve (MSC) developed in 1996 by Su and Johnson [10]; the determination of such curve requires a minimum set of experiments to describe the sintering process. MSC provides a measure of the densification of a material, within the conditions of a specific density range and is unique for a given material processed in a specific manner [11]. This method has been applied to the classical sintering of powder for a wide variety of metals such as iron [2] stainless steel (two-phase MSC for 17–4pH stainless steel [12], 316 L stainless steel [13,14]), nickel [15], tungsten [16] as well as ceramics like alumina [17], zirconia [10].

* Corresponding author.
E-mail address: manchili@chalmers.se (S.K. Manchili).

https://doi.org/10.1016/j.powtec.2021.06.052

Also, the MSC concept has been adopted for processes like pressure-assisted sintering of alumina [18], spark plasma sintering of UO_2 and UO_2-SiC [19]. The MSC method is reliant on the experimental data which makes it practical and convenient. Still, although MSC approach has been applied to variety of materials, most of the reported studies deal with unimodal size distribution of powder.

In this study, micro/nano bimodal iron powder mixtures have been examined. Two different micrometre sized iron powder were studied, with varying ratios of iron nanopowder additions. The compaction and sintering behavior for the different micro/nano bimodal iron powder mixtures was evaluated, and the relevant master sintering curves for each powder mixture were developed. The aim of study is to explore the compromise between the expected lowering of the sintering activation by nano-powder addition and potential negative impact on green density prior to sintering. It envisaged that the bimodal size distribution of powder, composed of the mixture of base micrometre sized powder with an optimized addition of nanopowder as sintering aid could be utilised for future manufacturing of structural components requiring higher density, such as gears and shafts for automotive applications. The study is part of a larger frame of research aiming to achieve full density in PM components produced through press and sinter route using water-atomized steel powder as base powder material. To explore the MSC curve approach from a theoretical point of view, commercially available carbonyl powder, having a relatively fine particle size (<5 μm) with high specific surface energy, was used as base powder with additions of the iron nanopowder. Then, water-atomized iron powder (<45 μm), being coarse in comparison to the carbonyl powder, but still having smaller average particles size than mainstream water-atomized iron powder (<150 μm) was used. The choices of experimental materials were selected to provide the necessary test matrix for the development and assessment of MSC for sintering of iron/steel powder compacts with nanopowder addition. There have been studies regarding the anisotropic sintering behavior [20], including the authors own unpublished work [21] where the impact of uniaxial compaction was shown on sintering. However, for the context of the current work and specifically for the application of MSC approach, isotropic shrinkage phenomenon is considered.

1.1. Master sintering curve model

Sintering is a thermally activated process that involves mass transport resulting in metallurgical bond formation between the metal powder particles. The driving force for sintering is to reduce or lower surface energy associated with the high specific surface area of the powder particles. For solid state sintering, atomic movement by diffusion is of importance. This movement of atoms can occur via the surface, grain boundaries or through the bulk of the powder particles or grains, once bonding has occurred. When the surface transport mechanisms are active, there is only bond formation between the particles, but the centers of the particles are not drawn closer to another. For the case of grain boundary and lattice diffusion mechanisms, being bulk transport mechanisms, the centers of the particles are drawn closer, thereby increasing the density of the compact. When the centers are drawn closer, there is an observable change in the dimension of the compact. A volumetric change is then noticed as the sintering densification occurs, through which the change in density could also be depicted. To predict the dimensional and subsequent density changes owing to the mass transport mechanisms during sintering, a combined stage sinter model was developed by Hansen et al. [22]. The master sintering curve (MSC) approach relies on fitting experimental data to the MSC model, although it is derived from the combined sinter stage model. Densification of the compact or the linear shrinkage rate is linked to the dominant diffusion mechanisms that operate, grain boundary and volume diffusion, resulting in the equation [23], showing the instantaneous linear shrinkage rate for the combined stage sintering model given by:

$$-\frac{dL}{Ldt}=\frac{\gamma\Omega}{kT}\left[\frac{\Gamma_V D_V}{G^3}+\frac{\Gamma_b\delta D_b}{G^4}\right] \tag{1}$$

where L is the dimension of the compact, t is the time, γ is the surface energy, Ω is the atomic volume, k is Boltzmann's constant, T is the temperature, $\Gamma$is the lumped scaling factor; which comprises characteristics for the component with respect to driving force, mean diffusion distance and geometric features and mean grain diameter, while D is the diffusion coefficient, δ the thickness of the grain boundary and G is the mean grain diameter. The subscripts b and V represent grain boundary diffusion and volume diffusion, respectively.

Assuming isotropic shrinkage, the shrinkage rate can be expressed in relation to densification rate as below:

$$-\frac{dL}{Ldt}=\frac{d\rho}{3\rho dt} \tag{2}$$

where ρ is the density.

To overcome the challenges posed by the (a) variation in the values of diffusivities for grain boundary and volume diffusion and (b) experimental characterization of lumped scaling factors, Su and Johnson [10] rearranged the equation and divided it into two parts, density dependent material parameters on one side and process dependent parameters on the other side and thereby developed the expression as follows:

$$\int_{\rho_0}^{\rho}\frac{kG^n}{3\gamma\Omega\rho D_0\Gamma}d\rho=\int_{t_0}^{t}\frac{1}{T}\,exp\left(-\frac{Q}{RT}\right)dt \tag{3}$$

The right-hand side, however, depends only on activation energy (Q) and time-temperature profile. This part is commonly referred as work of sintering (Θ):

$$\Theta\,(t,T)=\int_{t_0}^{t}\frac{1}{T}\,exp\left(-\frac{Q}{RT}\right)dt \tag{4}$$

Densification parameter (ψ), is used to overcome the challenge when comparing materials with different green densities [15] and the densification ratio (Φ) is used for the linearization, see equation

$$\psi=\frac{\rho-\rho_0}{1-\rho_0} \tag{5}$$

Densification ratio (Φ) is given by:

$$\Phi=\frac{\rho-\rho_0}{1-\rho} \tag{6}$$

2. Materials and methods

2.1. Materials

Two micrometre sized grades of powder were used as the base powder in this study, a < 45 μm water-atomized iron powder (ASC 300, Höganas AB, Sweden) and a < 5 μm carbonyl iron powder. Pure iron nanopowder <100 nm (Sigma-Aldrich) was used as nanopowder. Carbonyl iron powder is produced through a thermochemical decomposition process, whereas ASC 300 as said is produced through the

Table 1
Particle size analysis of micro powder grades used for sintering experiments.

Powder	Particle size analysis, μm
ASC 300	D_{10}: 17.93, D_{50}: 33.00, D_{90}: 58.42
Carbonyl powder	D_{10}: 2.01, D_{50}: 4.42, D_{90}: 8.47

water atomization process. The D_{50} particle size of the different powder are given in Table 1.

The iron nanopowder was admixed with two other kinds of powder to prepare different mixtures using a tumbler mixer placed in a glovebox flushed throughout the process with 99.999% pure nitrogen. Mixing was carried out for 12 h. Mixing was carried out in the glove box to minimize the nanopowder contamination. Four different bimodal powder mixes were formulated with nanopowder content of 5, 25, 50 and 75 wt% for mixes with water-atomized iron powder and carbonyl iron powder, respectively.

3. Methods

Different powder mixes were characterised by means of scanning electron microscopy (SEM) using Carl ZEISS-LEO Gemini 1550, equipped with a field emission gun.

The powder mixes were compacted using a uniaxial compaction press at a pressure of 300 MPa. The compaction pressure was kept low in order to produce a powder compact that has sufficient green strength to be handled, while, at the same time minimizing the impact of compaction on the sintering behavior. Compaction increases the coordination number and contact area between the particles, as well as induce dislocations in the crystal structure inside the individual powder particles. This has been shown to influence the sintering behavior of compacted metal powder [24].

The compacts were cylindrical disks of 10 mm diameter and 4 mm height. Sintering was conducted using a DIL 402C horizontal push rod dilatometer (Netzsch Thermal Analysis GmbH, Germany: DIL) under 99.9999% hydrogen gas atmosphere. The dimensional change was recorded in the direction parallel to the compaction direction. The target sintering temperature was 1350 °C with the isothermal holding time of 1 h. Though well above what is used in industrial-scale, sintering temperature of 1350 °C was chosen to study the entire range of sintering. To analyze the densification behavior, the dilatometric sintering was performed with heating rates of 2, 5 and 10 °C/min.

The green density of the compacts was calculated from the measured mass and volume of each compact. A micrometre was used to measure the height and the diameter of the cylinder, from which the volume of the compact was calculated. The simple balance was used to measure the mass of the compact, to an accuracy of 0.0001 g. Density of the sintered compacts was measured using Archimedes principle. Optical microscopy was carried out using a Zeiss Axioscope 7.

3.1. Treatment of dilatometric data

The MSCs for different powder combinations were developed from the dilatometric data. As a primary step towards the development of MSC, the raw data was processed in order to eliminate the thermal expansion from the data. The density at each data point was derived assuming that the sample undergoes isotropic shrinkage [15].

Corrected shrinkage data was obtained by means of the following equation:

$$\varepsilon'' = \varepsilon' - \alpha_m \widetilde{\rho}^{\frac{1}{3}} (T - T_0) \tag{7}$$

where ε' is the shrinkage obtained from dilatometry, α_m is the coefficient of thermal expansion, $\widetilde{\rho}$ is the relative density, T is the temperature and T_0 is the temperature at the initial condition.

4. Results and discussion

4.1. Powder compaction behavior

4.1.1. Carbonyl powder

The micrometre/nanosized bimodal powder mixture produced from carbonyl powder and nanopowder is shown in Fig. 1. The morphology of the micrometre and nanosized powder variants was observed to be spherical. During the tumbler mixing, the micrometre particles act as balls and disintegrate the nanopowder agglomerates. Through this, nanopowder distributed well and the agglomeration was reduced. Higher packing density is then achieved for powder mix as the fine nanosized particles fill the gaps between the large metal particles. German presented the equation to estimate the packing density with an assumption of an ideal mixture [25], which can be used as basis for depicting this effect with a size ratio between large/small particles greater than 7 being a critical criterium improved packing.

The green density in terms of relative theoretical density, as shown in Fig. 2, initially increases with the increase in the amount of

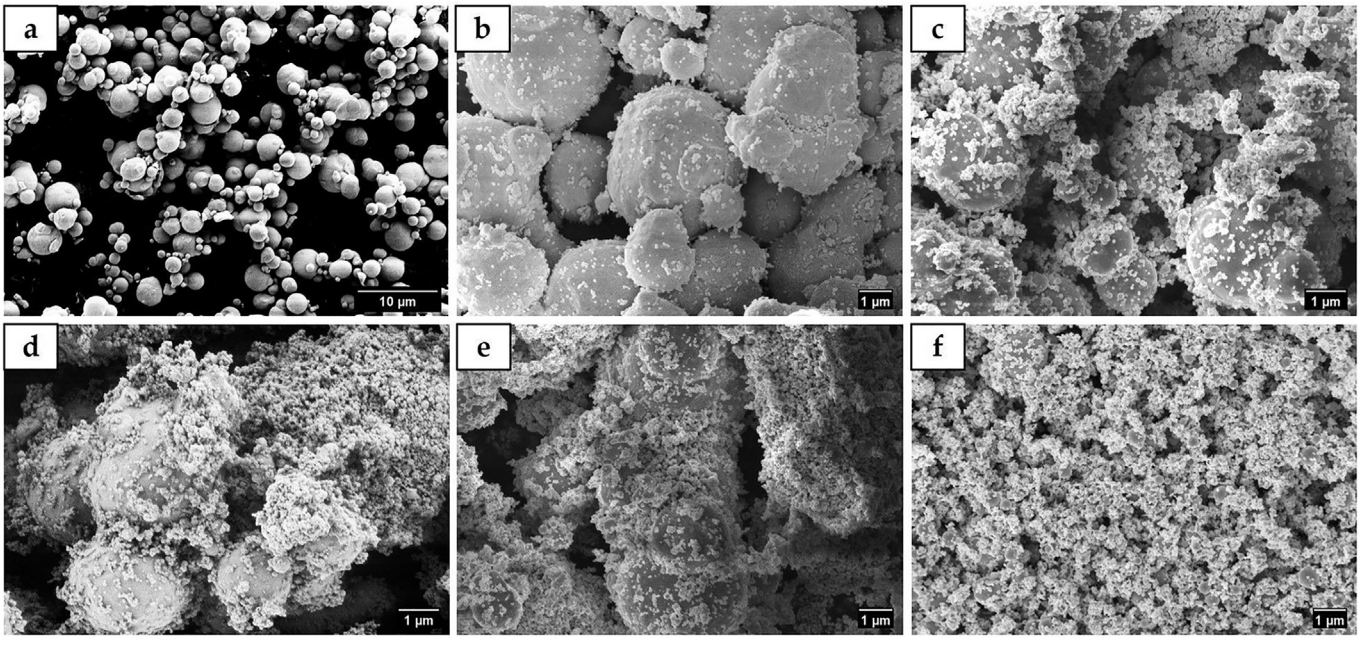

Fig. 1. SEM images of the powder (a) carbonyl, (b) C + 5%, (c) C + 25%, (d) C + 50%, (e) C + 75% and (f) nanopowder.

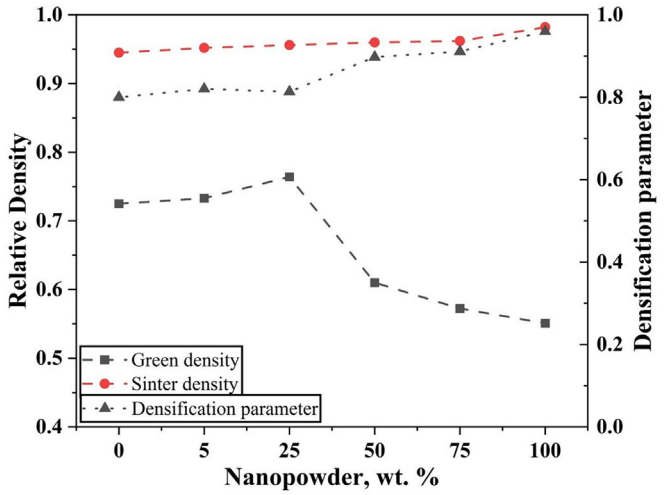

Fig. 2. Relative density and densification parameter of carbonyl compacts with varying amounts of nanopowder after compaction at 300 MPa.

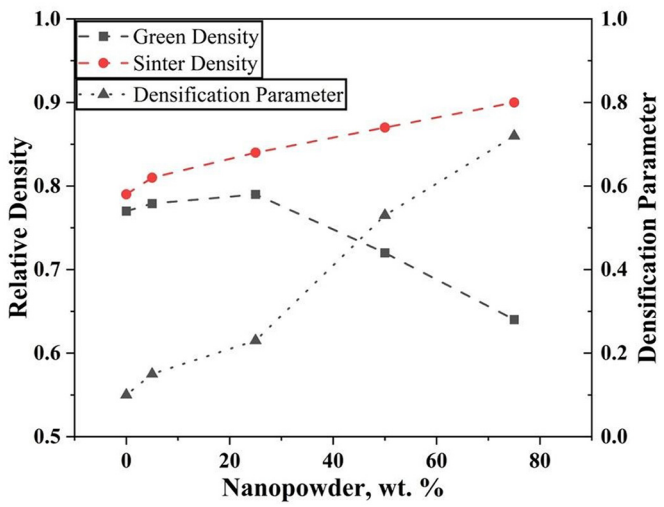

Fig. 4. Relative density and densification parameter of water-atomized iron powder (ASC 300) compacts with varying amounts of nanopowder.

nanopowder and then eventually decreases when nanopowder content reaches above an optimum level. The maximum green density of 76% (0.76 relative density) was hence obtained for powder mix containing 25 wt% nanopowder. This shows that the nanopowder effectively filled the spaces between the micrometre sized powder. The compact containing only nanopowder had the lowest relative density of 0.55 after compaction. This could be explained through the resistance offered by nanopowder to the compaction process [26].

4.1.2. Water atomized powder

Water-atomized iron powder of type ASC 300 combined with nanopowder in different weight fractions is shown in Fig. 3. The irregular morphology of the iron powder, a characteristic of water atomization process, can be seen from Fig. 3a. The water-atomized powder being irregular in shape allowed as well the nanopowder to fill well in between the particles. Then, the irregular morphology helped in retaining the nanopowder on its surfaces and also between the particles during the subsequent compaction [27]. As seen from Fig. 4, the maximum green density of 79% (0.79 relative density) was obtained for compact with 25 wt% nanopowder containing compact. Consequently, the initial increase and subsequent decrease in green density with the addition of nanopowder showed similar trend for compacts with both carbonyl iron and water-atomized iron powder base powder.

4.2. Sintering behavior

4.2.1. Carbonyl powder without and with added nanopowder

Sintered density values, in terms of relative density, are shown in Fig. 2 and Table 2. Samples heated at slow heating rate exhibited higher sintered density because they were exposed to thermal energy for a longer period. The sintered density increased with the increase in the amount of nanopowder. For the compact without nanopowder, the sintered density was 0.94, while this increased to 0.95 on addition of

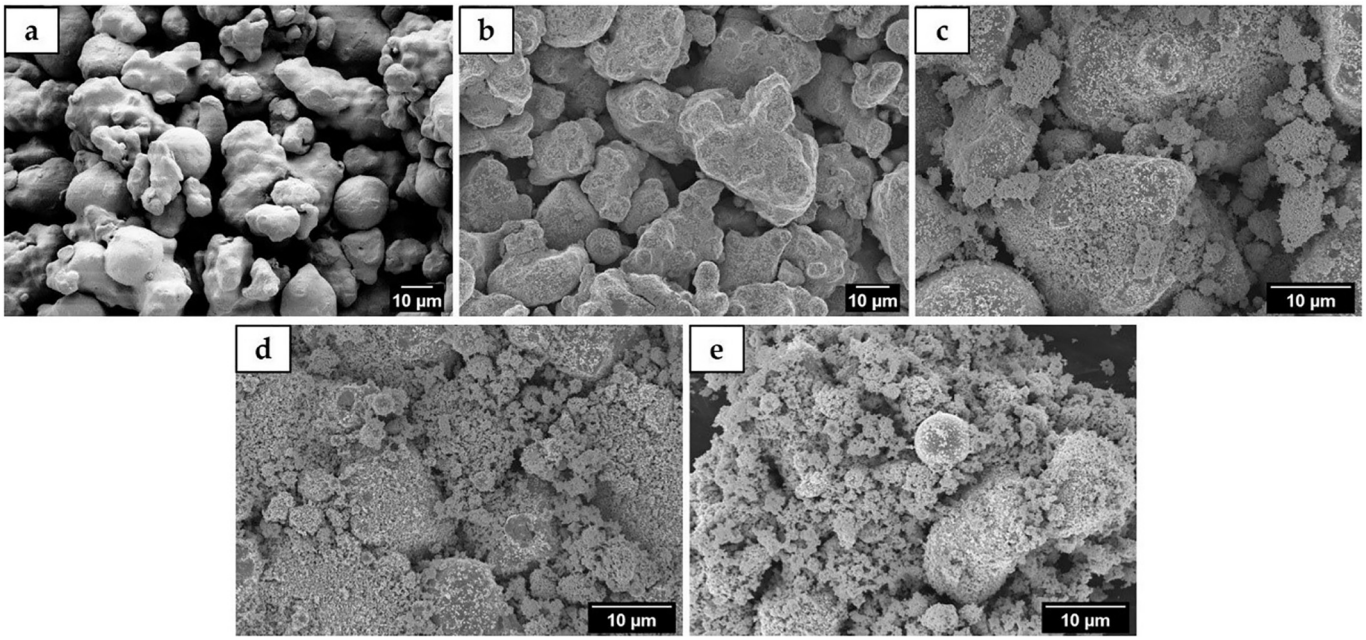

Fig. 3. SEM images of the powder (a) ASC 300, (b) ASC + 5%, (c) ASC + 25%, (d) ASC + 50%, and (e) ASC + 75%.

Table 2
Relative sintered density and densification parameter for carbonyl compacts.

Sample	Relative green density	Relative sintered density	Densification parameter
Carbonyl	0.72 ± 0.05	0.94 ± 0.05	0.8
C + 5%	0.73 ± 0.03	0.95 ± 0.02	0.81
C + 25%	0.76 ± 0.04	0.95 ± 0.06	0.82
C + 50%	0.61 ± 0.01	0.96 ± 0.01	0.89
C + 75%	0.57 ± 0.02	0.96 ± 0.02	0.91
Nanopowder	0.55 ± 0.01	0.98 ± 0.02	0.96

5 wt% nanopowder. For the compact with 25 wt% nanopowder, the sintered density was 0.95. For the compacts with 50 and 75 wt% nanopowder, the sintered density values were 0.96 and 0.98, respectively. As the green density is different for the compacts, the effect of nanopowder addition between the compacts would be difficult to analyze in terms of sintered density. Thus, densification parameter, ψ, [14] is used for depicting the net effect of nanopowder content. It could be seen from Fig. 2 that the densification parameter is 0.8 for compacts without nanopowder and 0.82 for both types of compacts with 5 and 25 wt% nanopowder. On further increasing the nanopowder content, the densification parameter value increases indicating an increase in the degree of sintering densification.

Compact containing nanopowder alone had the highest sintered density. Nanopowder, owing to the excess surface energy, is expected to sinter well in comparison to the micrometre sized powder alone. This helps in providing a dense grain boundary network around the micrometre powder and this grain boundary network provide diffusion path for the mass transport around and to the micrometre sized powder. As a consequence, there is an accelerated sintering [28] and hence the increase in sintered density. The fine particle size of the carbonyl powder itself also promotes sintering which helps in cumulatively increasing the density of this type of bimodal powder compacts.

Fig. 5 shows the microstructure of the samples sintered at 2 °C/min. The amount of residual porosity appeared to correlate to the increase in sintered density. Porosity decreased with an increasing amount of nanopowder and the compacts with nanopowder alone exhibited the smallest porosity.

Fig. 6 depicts the dilatometry shrinkage, which elucidates sintering behavior of different compacts ranging from no nanopowder to pure nanopowder. The graphs show shrinkage rate as a function of temperature during heating. It should be noted that the shrinkage values in Fig. 6 are not adjusted for thermal expansion as per Eq. (7). Compacts made from powder with no nanopowder additions showed conventional sintering behavior, as seen in Fig. 6a. The single peak at around 910 °C depicts the phase transformation from ferrite (*bcc*) to austenite (*fcc*). This peak in shrinkage rate was observed for all the compacts. For the variant with 5 wt% nanopowder, a minor peak in shrinkage rate at 820–870 °C was also seen (Fig. 6b). A minor peak appeared also at 400–450 °C with the increase in nanopowder content to 25 wt% (Fig. 6c). For the compact with 50 wt% nanopowder, along with the peak at 400–450 °C, a peak at 650 °C also appeared (Fig. 6d), while the peak at 820–870 °C disappeared. On further increasing the nanopowder content to 75 wt%, the peak positions remained similar (Fig. 6e). For the compact with only nanopowder, multiple peaks appeared at around 350 °C, 500 °C and 800 °C apart from the phase transformation peak at 910 °C (Fig. 6f).

4.2.2. Water atomized iron powder without and with added nanopowder

Various density values, in terms of relative sintered density, are shown in Table 3 and Fig. 4. For the compact without nanopowder, the relative sintered density was 0.79 whereas the addition of 5 wt % nanopowder increased the sintered density to 0.81. Increasing the nanopowder content from 25 to 50 wt%, meant that the relative sintered density increased from 0.84 to 0.87. Finally, for the compact with 75 wt% nanopowder, relative sintered density was 0.90. Densification parameter then increased from 0.1 for compact without nanopowder to 0.7 for the compact with 75 wt% nanopowder.

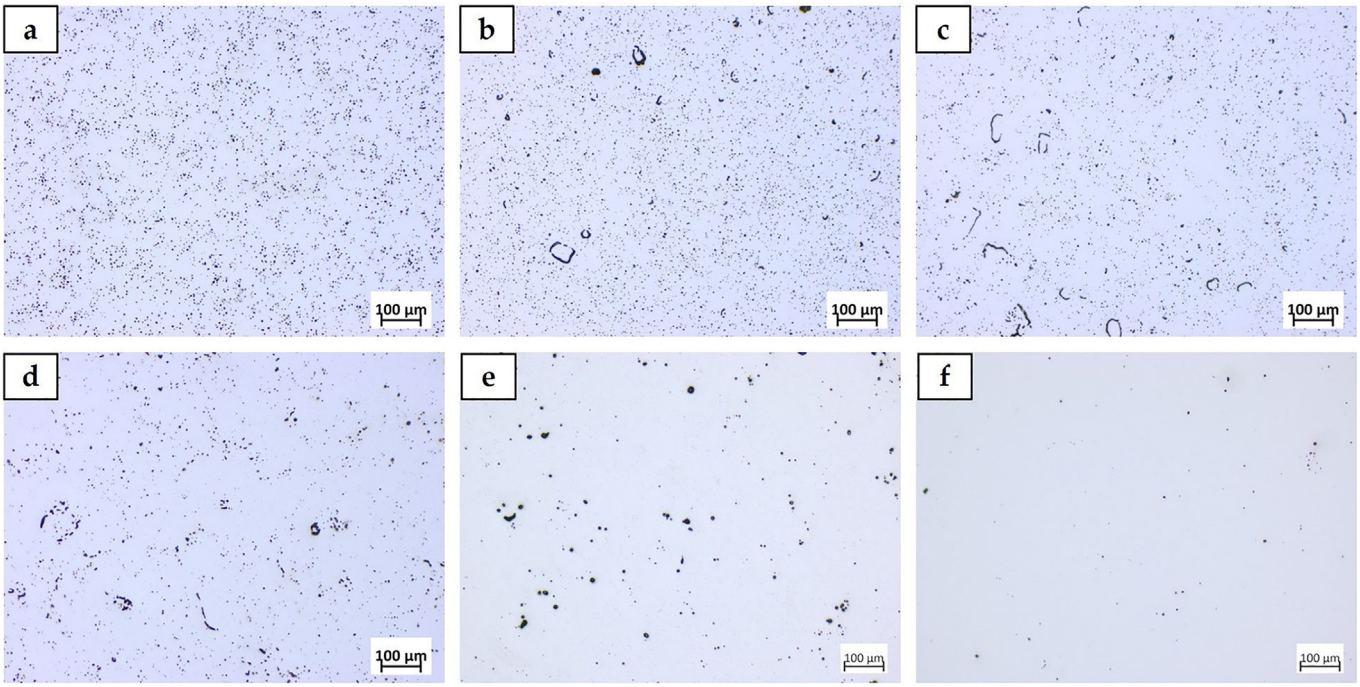

Fig. 5. Optical images of sintered samples with the heating rate of 2 °C/min (a) carbonyl powder only, (b) and with 5%, (c) 25%, (d) 50%, and (e) 75% nanopowder contents as well as (f) nanopowder only.

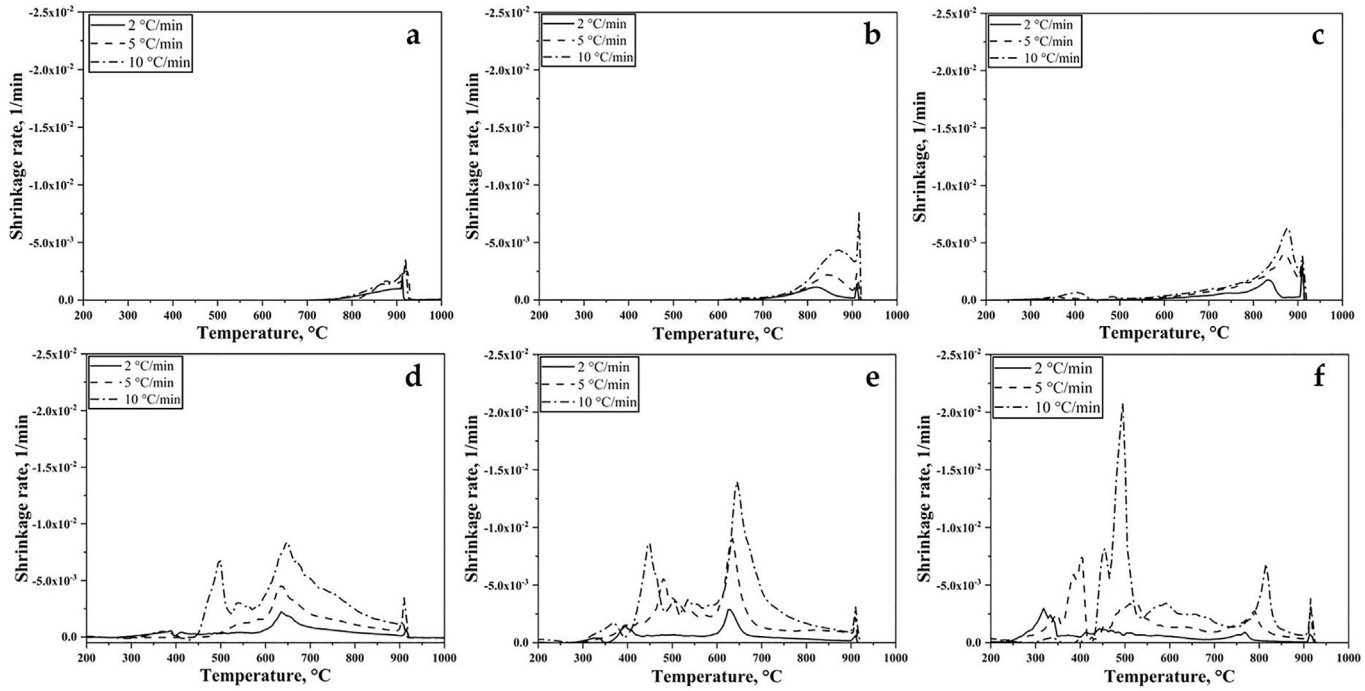

Fig. 6. Sintering behavior of different powder compacts at different heating rates (a) carbonyl powder, and with (b) 5%, (c) 25%, (d) 50% and (e) 75% nanopowder content as well as (f) nanopowder only.

Table 3
Relative green and sinter densities and densification parameter for compacts composed of water-atomized iron powder and nanopowder sintered at 2 °C/min.

Sample	Relative green density	Relative sintered density	Densification parameter
ASC 300	0.77 ± 0.05	0.79 ± 0.08	0.1
ASC + 5%	0.78 ± 0.01	0.81 ± 0.06	0.15
ASC + 25%	0.79 ± 0.09	0.84 ± 0.06	0.23
ASC + 50%	0.72 ± 0.01	0.87 ± 0.01	0.53
ASC + 75%	0.64 ± 0.02	0.90 ± 0.02	0.72

Fig. 7 shows the optical micrographs of cross-sections of sintered compacts composed of water-atomized iron powder and different amounts of nanopowder. The sintering hold was done at 1350 °C in pure hydrogen atmosphere with a heating rate of 2 °C/min. The porosity values assessed by the optical microscopy was consistent with the sintered density values by Archimedes principle measurements.

Fig. 8 shows the dilatometry shrinkage as a function of temperature during heating stage, which depicts the sintering behavior of compacts composed of water-atomized iron powder and different additions of

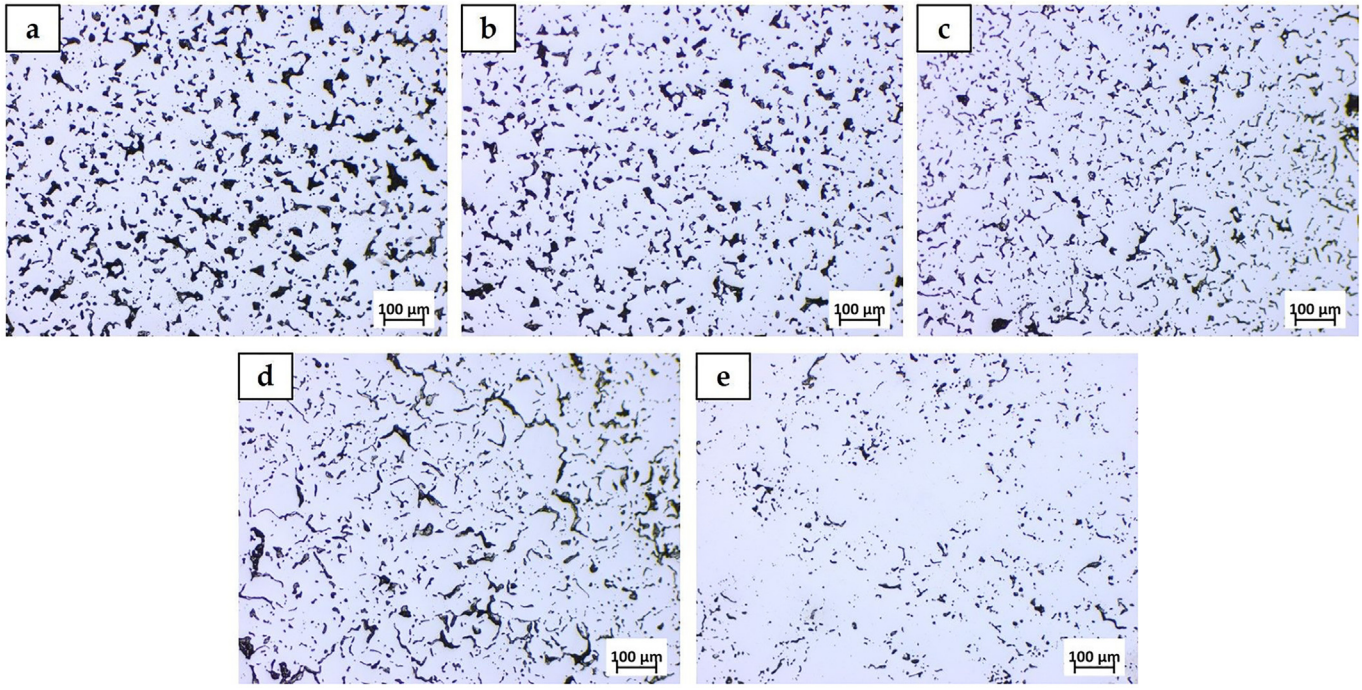

Fig. 7. Optical images of sintered compacts with the heating rate of 2 °C/min (a) water-atomized iron powder only, (b) and with 5%, (c) 25%, (d) 50% and (e) 75% nanopowder content.

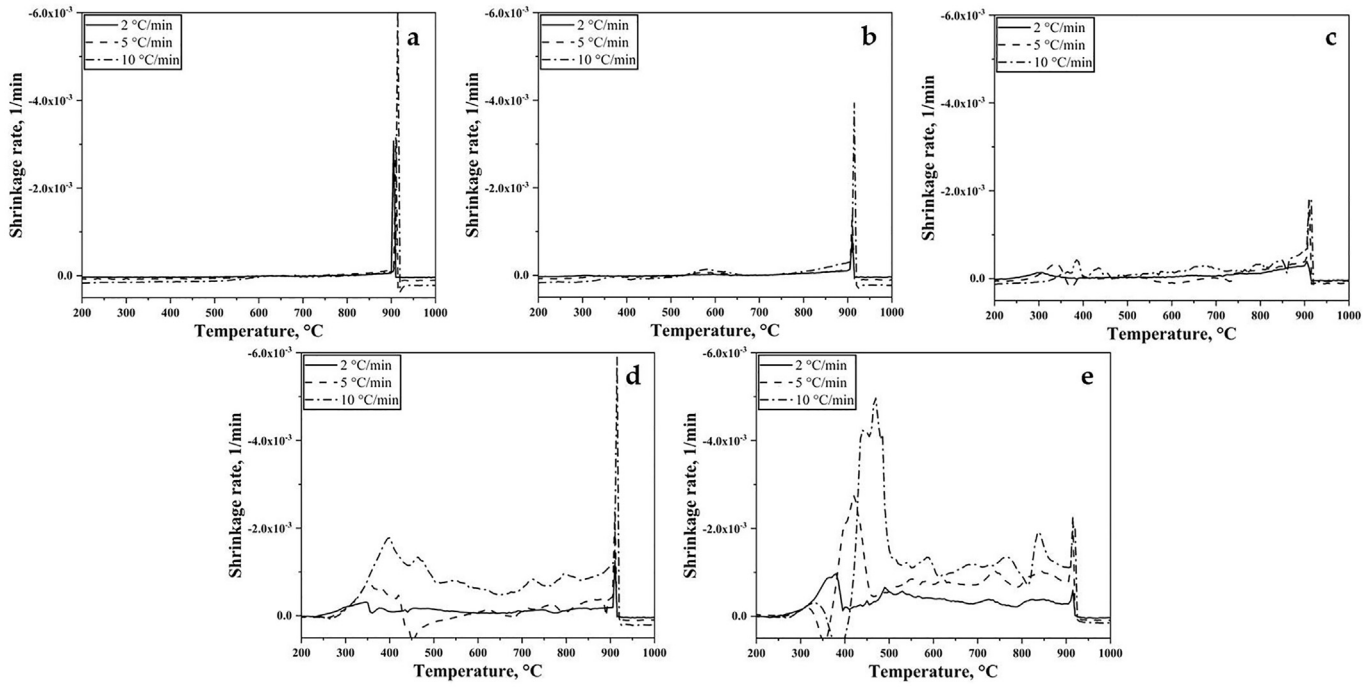

Fig. 8. Sintering behavior of powder compacts at different heating rates (a) water-atomized powder only, (b) and with 5%, (c) 25%, (d) 50% and (e) 75% nanopowder content.

nanopowder. The dilatometry shrinkage data in Fig. 8 has not been adjusted for thermal expansion as per Eq. (7). For the compacts without nanopowder, see Fig. 8a, conventional behavior was observed. The shrinkage rate peak at 910 °C corresponds to the ferrite (*bcc*) to austenite (*fcc*) transition. With the addition of 5% nanopowder, a small peak was also observed at 570 °C for the compacts sintered at the heating rate of 10 °C/min (Fig. 8b) apart from the phase transformation related peak at 910 °C, which was present for all the compacts. For the compact with 25% nanopowder, additional peaks appeared at temperatures as low as 350 °C (Fig. 8c). On further increasing the nanopowder content to 50%, additional peaks started to appear at 800 °C (Fig. 8d). For the compacts with 75% nanopowder, multiple peaks were observed at 450, 600 and 850 °C (Fig. 8e).

The peak temperatures in Figs. 6 and 8 show where the shrinkage rate is at a local maximum. This is the point where the change in shrinkage with time highest. The peak at the phase transformation temperature associated with phase change is due to the volumetric size change from body centered cubic (BCC) structure to face centered cubic (FCC) structure. The diffusion in FCC-austenite, a close packed crystal structure, takes place at a slower rate and therefore the sintering shrinkage rate is slower in austenite phase compared to BCC-ferrite.

Fig. 9 and Table 4 summarize the peak shrinkage temperatures for the compacts based on the carbonyl powder and water-atomized iron powder (ASC300) including the variants with different nanopowder content sintered at 10 °C/min. It is obvious that the nanopowder influences the sintering behavior. As the nanopowder content increased, the temperature at which densification initiated decreased. Therefore, the sintering of nanopowder occurs as expected at temperatures lower than that of micrometre sized powder [29]. The large specific area of nanopowder is associated with increased excess surface energy and hence higher sintering activity [4,30]. As the nanopowder content increased, the compacts revealed a two-peak shrinkage rate behavior apart from the phase transformation peak. Such behavior is typically observed for nanopowder [31]. The double sintering rate peaks observed are explained through intra-agglomerate sintering and inter-agglomerate sintering [32]. The peak for the low temperature region signifies the sintering of nanopowder within the agglomerate, which results in reduction in intra-agglomerate porosity. The height of the peak

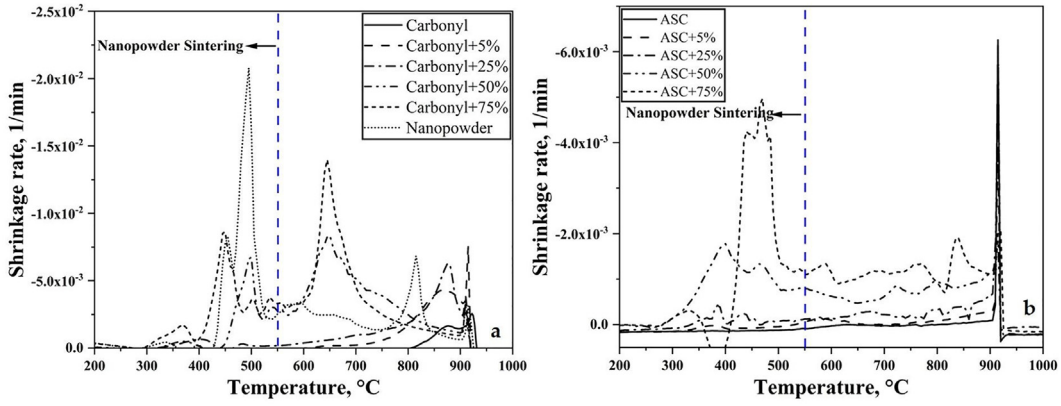

Fig. 9. Shrinkage behavior of (a) carbonyl-based compacts and (b) water atomized (ASC 300) powder-based compacts with varying nanopowder content sintered at 10 °C/min.

Table 4
Temperatures for the different shrinkage peak recorded in the dilatometer studies at 10 °C/min.

Sample	Shrinkage peak temperature, °C	Sample	Shrinkage peak temperature, °C
Carbonyl iron (C)	910	Iron powder (ASC)	910
C + 5%	850, 910	ASC + 5%	570, 910
C + 25%	400, 850, 910	ASC + 25%	375, 910
C + 50%	470, 650, 910	ASC + 50%	375, 800, 910
C + 75%	450, 650, 910	ASC + 75%	475, 850, 910
Nanopowder	500, 810, 910		

was found to increase with increasing nanopowder content in the present study. The second peak represents the reduction of inter-agglomerate porosity. Sintering between the nanopowder agglomerates is thus given by this peak. The position of the two kinds of peaks changed with nanopowder content. One of the reason could be that nanopowder sinters to the micrometre sized powder and pulls its particles together which in turn increases the contact surface between them therefore this improves overall densification [33].

4.3. Master sintering curve

4.3.1. Calculation of apparent activation energy for sintering

It has been established that the work of sintering is a function of time, temperature and apparent activation energy (Eq. (8)). Apparent activation energy values are not directly obtained from dilatometric data. Therefore, this has to be obtained before venturing into the construction of MSC. In this study, the mean residual method, given by the equation presented by Oh et al. [2], was used to obtain the activation energy as follows:

$$\text{Mean residual square} = \sqrt{\frac{1}{\rho_f - \rho_0}\int_{\rho_0}^{\rho_f} \frac{\sum_{i=1}^{N}\left(\frac{\Theta_i}{\Theta_{i-avg}} - 1\right)^2}{N} d\rho} \quad (8)$$

where ρ_f is the final density, ρ_0 is the initial density, N is the number of experimental data points, and Θ_{i-avg} is the average value of all the work of sintering over *N*. For the correct activation energy value, each Θ vs. ρ curve should be a single sigmoidal curve [15]. Hence, the apparent activation energy was determined by minimizing the mean residual square.

Table 5
Apparent activation energy for both water atomized (ASC 300) and carbonyl powder compacts.

Material	ASC 300	+5%	+25%	+50%	+75%	Nanopowder
Apparent activation energy (kJ/mol)	356	347	322	298	260	158
Material	Carbonyl	+5%	+25%	+50%	+75%	
Apparent activation energy (kJ/mol)	320	315	304	281	208	

Fig. 10 shows the determination of activation energy for water atomized (ASC 300) powder using three different heating rates. The best estimation for apparent activation energy for the ASC 300 compact was found at 356 kJ/mol with a minimum residual square. The apparent activation energy values used in this study obtained for both water atomized (ASC 300) and carbonyl based bimodal powder compacts are summarized in Table 5.

Table 5 shows that the activation energies decreased with the increase in nanopowder content. As it is already said, sintering activation energy is the minimum energy required to initiate the sintering process. Thus, smaller activation energy signifies that the process of sintering is initiated at lower temperature. This is due to the large specific surface area which contributes to more contact regions for better diffusion and hence decreases activation energy values. It should be noted that the value of the dimensionless mean residual square value reflects the quality of experimental data, with a low value showing a closer correlation.

As mentioned earlier, the MSC is a form of relationship between relative density and work of sintering which can described as a sigmoidal function. Fig. 11 shows the linearized form of MSC from which sigmoidal parameters were calculated. The details for the calculation of sigmoidal parameters are given in Appendix. The parameter values were influenced by the nanopowder variation. Though the axes for MSC is relative density and work of sintering, densification parameter was used instead of density as the initial conditions of the compacts were different from one another other.

The MSCs were constructed using the activation energy values calculated from mean residual square method and the sigmoidal parameters for both carbonyl-based and water atomized (ASC 300)-based compacts (Fig. 12). The lower the value of work of sintering is, the higher is the energy needed for the process. Work of sintering

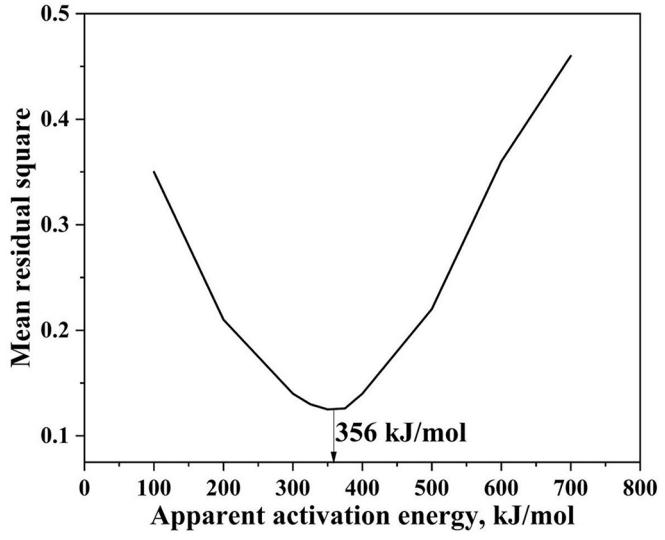

Fig. 10. Apparent activation energy determination through mean residual square method for water-atomized iron (ASC300) powder compacts.

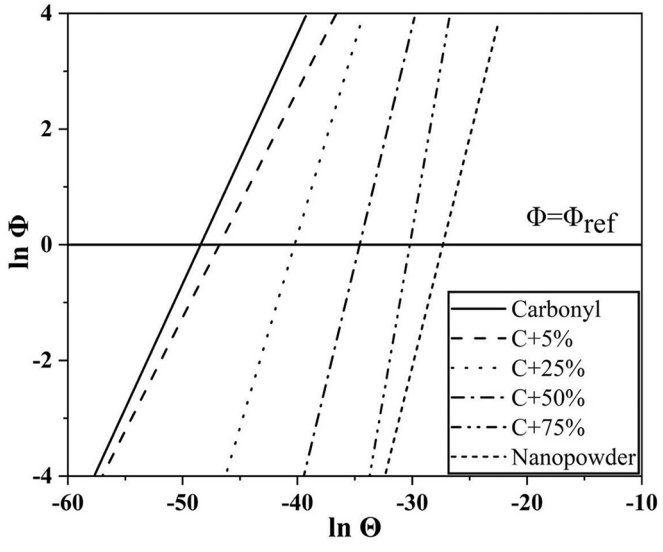

Fig. 11. Linearized master sintering curve for carbonyl powder based compacts.

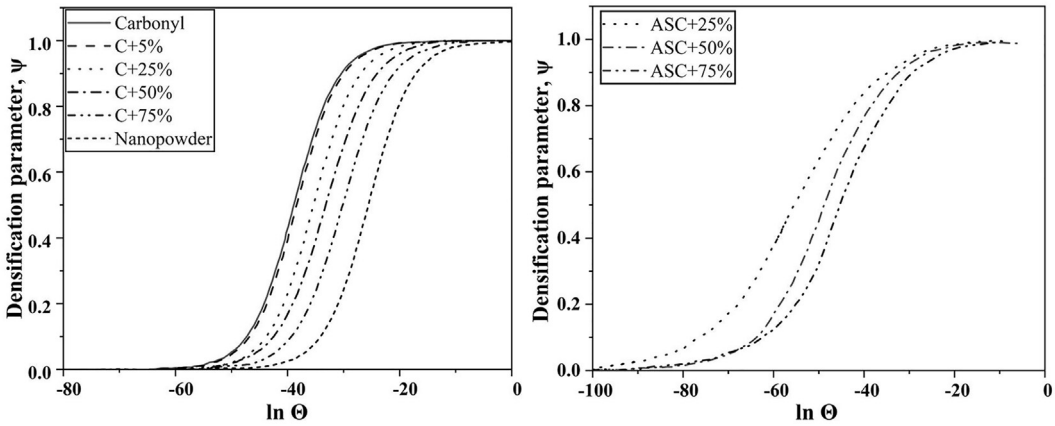

Fig. 12. Master sintering curve of (a) carbonyl powder compacts and (b) water atomized (ASC 300) powder compacts.

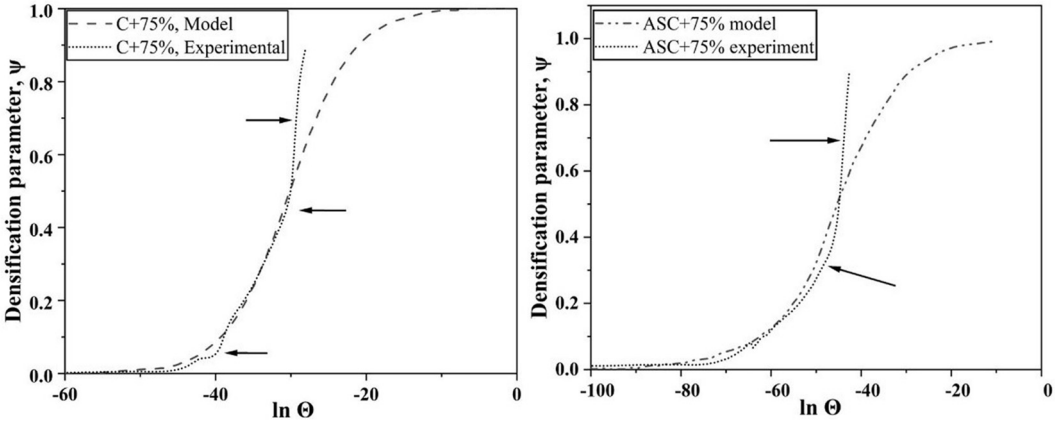

Fig. 13. Master sintering curve with experimental result of compacts composed of (a) carbonyl iron and 75 wt% nanopowder and (b) water atomized (ASC 300) iron powder and 75 wt% nanopowder.

represents the energy needed to densify the green body. It could be seen from the figure that as the nanopowder content increased, work of sintering also increased. The experimental results shown in Fig. 13 differ from the model for the compacts with 75% nanopowder. Such difference was observed for all the compacts between the model and experimental MSCs. This could be an effect of the two-peak sintering rate nature of the compacts; not being depicted from the conventional MSCs as they are developed for single peak behavior of traditional micrometre sized powder. It seems that the intra/interagglomerate sintering kinetics associated with nanopowder is the governing influence in this study which contribute to the difference between the model and experimental MSCs. It has also been suggested, to employ the two-stage sintering model for better overlap between the experiments and model MSCs. Such model is beneficial for materials that undergo phase transformations. Therefore, by differentiation between the regions with respect to phase transition, the accuracy of the model could be improved [2,12]. However, MSCs could not be constructed for the ASC 300 and ASC 300 + 5 wt % nanopowder compacts as the obtained shrinkages for these compacts were too small to construct meaningful MSC.

5. Conclusions

In this study, sintering behavior of different bimodal powder variants produced by mixing micrometre sized and nanopowder was investigated. The micrometre sized base powder used were of two kinds; irregularly shaped and correspondingly coarser water-atomized iron powder and finer carbonyl iron powder, while pure nanopowder with particle size of maximum 100 nm was studied as sintering aid. The green density was measured for all the compacts, produced through press and sinter route, ranging from micrometre sized powder only to mixtures with 5, 25, 50 and 75 wt% nanopowder and pure nanopowder only compacts. The compact containing 25 wt% nanopowder had highest relative green density for both compacts of both kinds of mixtures, estimating at 0.76 and 0.79 for carbonyl and water atomized iron powder, respectively. The densification parameter increased with increasing nanopowder content; attributed to the dense grain boundary network promoted by the nanopowder sintering resulting in enhanced densification. The bimodal powder and nanopowder showed multi peak shrinkage rate behavior, supposed to be explained by the intra-agglomerate and inter-agglomerate sintering of nanopowder. In this study, the conventional master sintering curve concept was applied compacts consisting of water atomized iron powder mixed with varying amounts nanopowder. The compacts composed of carbonyl powder mixed with nanopowder was used to understand the application of master sintering curve to sinter compacts; to be applied to the compacts based on water atomized iron powder. The activation energy values for sintering of each kind of powder were calculated using mean square residual method. The shape of the curve was influenced by the amount of nanopowder added as the work of sintering increased with increasing nanopowder content. The curves showed relatively large errors because of their multi-peak shrinkage behavior. The amount of error was high in the case of water atomized iron powder compacts in comparison to carbonyl powder compacts.

Declaration of Competing Interest

The authors declare that they have no known competing financial interests or personal relationships that could have appeared to influence the work reported in this paper.

Acknowledgements

This work has been carried out within the project 'Nanotechnology enhanced sintered steel processing' through support from Swedish Foundation for Strategic Research, SSF within the program 'Generic Methods and Tools for Future Production'. The authors would like to acknowledge the support from 'Area of Advance, Production', Chalmers University of Technology and Höganäs AB, Sweden for the scientific and technical co-operation. Funding from the strategic innovation program LIGHTer, provided by Vinnova, is also gratefully acknowledged.

Appendix A

Combining (1, 2) gives:

$$\frac{d\rho}{3\rho dt} = \frac{\gamma\Omega}{kT}\left[\frac{\Gamma_V D_V}{G^3} + \frac{\Gamma_b \delta D_b}{G^4}\right] \tag{A.1}$$

Since the diffusivities are exponentially dependent on the temperature, Eq. (1) could be rewritten using Arrhenius functions [22,34] as follows:

$$-\frac{dL}{Ldt} = \frac{\gamma\Omega}{kT}\left[\frac{\Gamma_V D_{0V}}{G^3}\, exp\left(-\frac{Q_V}{RT}\right) + \frac{\Gamma_b \delta D_{0b}}{G^4}\, exp\left(-\frac{Q_b}{RT}\right)\right] \tag{A.2}$$

where D_0 is the pre-exponential factor, Q is the activation energy and R is the universal gas constant.
If the sintering phenomena are governed by a single diffusion mechanism (either grain boundary or volume diffusion), G and Γ are functions of density, ρ. Then, the above Eq. (A.2) can be rewritten as:

$$\frac{d\rho}{3\rho dt} = \frac{\gamma\Omega\Gamma(\rho)D_0}{kT(G(\rho))^n}\exp\left(-\frac{Q}{RT}\right) \tag{A.3}$$

where D_0 is the diffusion coefficient of the dominant diffusion mechanism; $D_0 = D_{0V}$ and $n = 3$ for volume diffusion whereas $D_0 = \delta D_{0b}$ and $n = 4$ for grain boundary diffusion.
The terms on the left-hand side of (3) are quantities which define microstructural evolution and material properties:

$$\phi(\rho) = \int_{\rho_0}^{\rho} \frac{kG^n}{3\gamma\Omega\rho D_0\Gamma} d\rho \tag{A.4}$$

Thus, in general form (3) becomes:

$$\phi(\rho) = \Theta\,(t, T) \tag{A.5}$$

The apparent activation energy value for sintering is now calculated through numerical analysis. For a given value of work of sintering, there exists a corresponding density condition as per Eq. (6). If the relationship between density and work of sintering is established, MSC describing this relationship is determined for a given sintering system.
The MSC is consequently the relationship between ϕ and ρ. As mentioned before, it is difficult to obtain Γ. The work of sintering could be calculated by integrating the heating cycle of the sintering process. A polynomial function was suggested for depicting an MSC by Johnson et al. [10]. A sigmoidal function was proposed by Teng et al. [35] and Blaine et al. [15] to describe the MSC. The sigmoidal function of an MSC can be expressed as a function of relative density and work of sintering as:

$$\widetilde{\rho} = \widetilde{\rho}_0 + \frac{1-\widetilde{\rho}_0}{1 + exp\left(-\frac{\ln\Theta - a}{b}\right)} \tag{A.6}$$

where $\widetilde{\rho}$ is the relative density, $\widetilde{\rho}_0$ is the initial relative density and the constants a and b are sigmoidal parameters. The parameter a coincides with the point of inflection of the curve and parameter b is the slope of the linearized curve.
Combining A.6 and (5) then gives:

$$\psi = \frac{\widetilde{\rho} - \widetilde{\rho}_0}{1-\widetilde{\rho}_0} = \frac{1}{1 + exp\left(-\frac{\ln\Theta - a}{b}\right)} \tag{A.7}$$

In the terms of work of sintering, the above equation is written as:

$$\Phi = \left(\frac{\Theta}{\Theta_{ref}}\right)^n \tag{A.8}$$

where Θ_{ref} is the work of sintering at $\widetilde{\rho} = \frac{1+\widetilde{\rho}_0}{2}$ and n is the power law exponent. The relationship between ψ and Φ is given by:

$$\frac{1}{\psi} = 1 + \frac{1}{\Phi} \tag{A.9}$$

The linearization of MSC is then finally given by the equation as follows:

$$\ln \Phi = \frac{1}{b}(\ln \Theta - a) = n(\ln \Theta - \ln \Theta_{ref}) \tag{A.10}$$

The sigmoidal parameters for different powder mixtures is given in Table A.1.

Table A.1
Sigmoidal parameters for different powder mixtures.

Material	a	b	Material	a	b
Carbonyl	−38.47	1.39	ASC 300 + 25%	−48.97	4.53
C + 5%	−37.89	1.43	ASC 300 + 50%	−45.73	4.46
C + 25%	−35.18	1.66	ASC 300 + 75%	−40.18	3.67
C + 50%	−31.15	1.93			
C + 75%	−29.15	2.45			
Nanopowder	−27.30	1.79			

In order to measure the sinterability of a compact over a wide density range, master sintering curve (MSC) approach is adopted.

A.1. Treatment of dilatometery data

The thermal expansion coefficients are obtained from the dilatometry data in the cooling step by calculating the relationship between the shrinkage and the temperature. The obtained values were in agreement with the ones reported previously, see [7,15]. These values were used to compensate for the thermal expansion effects during sintering. Once shrinkage without the thermal expansion is obtained, the next step is to calculate the relative density at each temperature.

Relative density at each temperature was calculated using the equation:

$$\widetilde{\rho} = \frac{\widetilde{\rho}_0}{(1+\varepsilon'')^3} \tag{A.11}$$

where, $\widetilde{\rho}_0$ is the relative green density and ε'' shrinkage at the given temperature.

References

[1] Höganäs, Design and Mechanical Properties, 2013.
[2] J.W. Oh, Y. Seong, D.S. Shin, S.J. Park, Investigation and two-stage modeling of sintering behavior of nano/micro-bimodal powders, Powder Technol. 352 (2019) 42–52, https://doi.org/10.1016/j.powtec.2019.04.056.
[3] J.W. Oh, R. Bollina, W.S. Lee, S.J. Park, Effect of nanopowder ratio in bimodal powder mixture on powder injection molding, Powder Technol. 302 (2016) 168–176, https://doi.org/10.1016/j.powtec.2016.08.051.
[4] J. Rajabi, N. Muhamad, A.B. Sulong, Effect of nano-sized powders on powder injection molding: a review, Microsyst. Technol. 18 (2012) 1941–1961, https://doi.org/10.1007/s00542-012-1631-9.
[5] D. Wei, R. Dave, R. Pfeffer, Mixing and characterization of Nanosized powders: An assessment of different techniques, J. Nanopart. Res. 4 (2002) 21–41, https://doi.org/10.1023/A:1020184524538.
[6] S.K. Manchili, J. Wendel, A. Zehri, J. Liu, E. Hryha, L. Nyborg, Effect of Nanopowder addition on the sintering of water-atomized Iron powder, Metall. Mater. Trans. A. (2020)https://doi.org/10.1007/s11661-020-05891-1.
[7] J.W. Oh, W.S. Lee, S.J. Park, Nanopowder effect on Fe Nano/micro-bimodal powder injection molding, Metall. Mater. Trans. A. 49 (2018) 5535–5545, https://doi.org/10.1007/s11661-018-4851-5.
[8] W.D. Kingery, M. Berg, Study of the initial stages of sintering solids by viscous flow, evaporation-condensation, and self-diffusion, J. Appl. Phys. 26 (1955) 1205–1212, https://doi.org/10.1063/1.1721874.
[9] R.L. Coble, Sintering crystalline solids. I. Intermediate and final state diffusion models, J. Appl. Phys. 32 (1961) 787–792, https://doi.org/10.1063/1.1736107.
[10] H. Su, D.L. Johnson, Master sintering curve: a practical approach to sintering, J. Am. Ceram. Soc. 79 (1996) 3211–3217.
[11] C.B. Diantonio, K.G. Ewsuk, Master sintering curve and its application in sintering of electronic ceramics, Sinter. Adv. Mater. (2010) 130–161, https://doi.org/10.1533/9781845699949.1.130.
[12] I.D. Jung, S. Ha, S.J. Park, D.C. Blaine, R. Bollina, R.M. German, Two-phase master sintering curve for 17-4 PH stainless steel, Metall. Mater. Trans. A. 47 (2016) 5548–5556, https://doi.org/10.1007/s11661-016-3687-0.
[13] D.Y. Park, S.W. Lee, S.J. Park, Y.-S. Kwon, I. Otsuka, Effects of particle sizes on sintering behavior of 316L stainless steel powder, Metall. Mater. Trans. A. 44 (2013) 1508–1518, https://doi.org/10.1007/s11661-012-1477-x.
[14] J.W. Oh, S.K. Ryu, W.S. Lee, S.J. Park, Analysis of compaction and sintering behavior of 316L stainless steel nano/micro bimodal powder, Powder Technol. 322 (2017) 1–8, https://doi.org/10.1016/j.powtec.2017.08.055.
[15] D.C. Blaine, S.J. Park, P. Suri, R.M. German, Application of work-of-sintering concepts in powder metals, Metall. Mater. Trans. A Phys. Metall. Mater. Sci. 37 (2006) 2827–2835, https://doi.org/10.1007/BF02586115.
[16] J. Almanstötter, Densification of potassium-doped tungsten during sintering, Int. J. Refract. Met. Hard Mater. 50 (2015) 217–220, https://doi.org/10.1016/j.ijrmhm.2015.01.017.
[17] V. Pouchly, K. Maca, Master sintering curve - a practical approach to its construction, Sci. Sinter. 42 (2010) 25–32, https://doi.org/10.2298/SOS1001025P.
[18] K. An, M.K. Han, Microstructural evolution based on the pressure-assisted master sintering surface, Mater. Sci. Eng. A 391 (2005) 66–70, https://doi.org/10.1016/j.msea.2004.08.055.
[19] Z. Chen, G. Subhash, J.S. Tulenko, Master sintering curves for UO2 and UO2–SiC composite processed by spark plasma sintering, J. Nucl. Mater. 454 (2014) 427–433, https://doi.org/10.1016/j.jnucmat.2014.08.023.
[20] H.E. Exner, E.A. Giess, Anisotropic shrinkage of cordierite-type glass powder cylindrical compacts, J. Mater. Res. 3 (1988) 122–125, https://doi.org/10.1557/JMR.1988.0122.
[21] J. Wendel, Sintering of Water-Atomized Iron and Low-Alloyed Steel Powder, Chalmers University of Technology, 2020.
[22] J.D. Hansen, R.P. Rusin, M. Teng, D.L. Johnson, I 35 (1992) 1129–1135.
[23] M. Mazaheri, A. Simchi, M. Dourandish, F. Golestani-Fard, Master sintering curves of a nanoscale 3Y-TZP powder compacts, Ceram. Int. 35 (2009) 547–554, https://doi.org/10.1016/j.ceramint.2008.01.008.
[24] R.M. German, Powder Metallurgy and Particulate Materials Processing: The Processes, Materials, Products, Properties and Applications, Metal Powder Industries Federation, https://books.google.se/books?id=04CnAQAACAAJ 2005.
[25] R.M. German, Prediction of sintered density for bimodal powder mixtures, Metall. Trans. A. 23 (1992) 1455–1465, https://doi.org/10.1007/BF02647329.
[26] O. Dominguez, M. Phillippot, J. Bigot, The relationship between consolidation behavior and particle size in Fe nanometric powders, Scr. Metall. Mater. 32 (1995) 13–17, https://doi.org/10.1016/S0956-716X(99)80003-X.
[27] A.B. Yu, N. Standish, A study of the packing of particles with a mixture size distribution, Powder Technol. 76 (1993) 113–124.
[28] J.-P. Choi, H.-G. Lyu, W.-S. Lee, J.-S. Lee, Densification and microstructural development during sintering of powder injection molded Fe micro–nanopowder, Powder Technol. 253 (2014) 596–601, https://doi.org/10.1016/j.powtec.2013.11.048.
[29] J. Rajabi, N. Muhamad, A.B. Sulong, A. Fayyaz, M.R. Raza, The effect of nano-sized stainless steel powder addition on mechanical and physical properties of micropowder injection molded part, Mater. Des. 63 (2014) 223–232, https://doi.org/10.1016/j.matdes.2014.05.071.

[30] Y. Kinemuchi, K. Watari, Dilatometer analysis of sintering behavior of nano-CeO2 particles, J. Eur. Ceram. Soc. 28 (2008) 2019–2024, https://doi.org/10.1016/j.jeurceramsoc.2008.02.003.
[31] P. Knorr, J.G. Nam, J.S. Lee, Densification and microstructural development of nano-crystalline γ-Ni-Fe powders during sintering, Nanostruct. Mater. 12 (1999) 479–482, https://doi.org/10.1016/S0965-9773(99)00163-4.
[32] S. Koley, A. Ghosh, A.K. Sahu, R. Tewari, A.K. Suri, Correlation of compaction pressure, green density, pore size distribution and sintering temperature of a nano-crystalline 2Y-TZP-Al2O3 composite, Ceram. Int. 37 (2011) 731–739, https://doi.org/10.1016/j.ceramint.2010.11.003.
[33] J. Song, G.-Y. Lee, E.-J. Hong, C.S. Lee, J.-S. Lee, Sintering behavior of bimodal iron nanopowder agglomerates, J. Am. Ceram. Soc. 102 (2019) 3791–3801, https://doi.org/10.1111/jace.16240.
[34] S.J. Park, J.M. Martin, J.F. Guo, J.L. Johnson, R.M. German, Densification behavior of tungsten heavy alloy based on master sintering curve concept, Metall. Mater. Trans. A Phys. Metall. Mater. Sci. 37 (2006) 2837–2848, https://doi.org/10.1007/BF02586116.
[35] M.-H. Teng, Y.-C. Lai, Y.-T. Chen, Computer program of master sintering modeling to accurately predict sintering results, West. Pacific Earth Sci. 2 (2002) 171–180.